Electronic Supplementary Material (ESI) for Journal of Materials Chemistry A.

Supporting Information

Kinetics enhanced hierarchical $Ni_2P_{1-x}S_x$/Ni@carbon/graphene yolk-shell microspheres boosting advanced sodium/potassium storage

Experimental Section

Uniform Ni-MOFs precursor spheres synthesis. All the chemicals were directly used after purchase without further purification. The hydrothermal method was followed to synthesize Ni-MOFs precursors.[1] Under vigorous magnetic stirring, a mixture of 0.605 g $Ni(NO_3)_2 \cdot 6H_2O$, 0.21 g trimesic acid, and 2.1 g of PVP-K30 (M_w = 40000) was dissolved in 42 mL mixture of DMF, ethanol, and water (1:1:1, v/v/v). Then the mixture was sealed in 70 mL Teflon-lined autoclave and heated to 150 °C for 10 h. Afterward, the green precipitate was washed by DMF and ethanol for several times and dried in a vacuum oven at 60 °C for 12 h.

Yolk−shell (YS) $Ni_2P_{1-x}S_x$/Ni@C/G *spheres synthesis.* The YS $NiP_{1-x}S_x$/Ni@C/G spheres were obtained via a one-step process. Briefly, 50 mg Ni-MOFs precursor spheres, and the mixture of red P and S powder were separately placed in two quartz boats, and the mixture of red P and S powder was placed at the upstream zone in a tube furnace. The varied mass ratio of P and S (2:1, 1:1, and 1:2) was first mixed with 80 mg of powder using mortar and pestle to synthesize samples with di□erent S/P ratios. Then, the furnace was set to increase up to 450 °C for 2 h with a ramp rate of 1 °C min^{-1} bypassing Ar atmosphere to obtain YS $Ni_2P_{1-x}S_x$/Ni@C/G microspheres. For comparison, the pure S powder and P powder replace the mixture of red P and S powder under the same above condition, respectively, were denoted as Ni_9S_8/Ni@C/G, and Ni_2P/Ni@C/G composites, respectively. Moreover, the Ni-MOF precursor was calcined in air at 420 °C for 3h with 1 °C min^{-1}, and the porous NiO was obtained. Then, 50 mg porous NiO was phosphated by 750 mg $NaH_2PO_2 \cdot H_2O$ at 350 °C for 2h to synthesize Ni_2P, and sulfided by 100 mg S power at 450 °C for 2h and then 600 °C 1h to prepare Ni_9S_8/NiS in Ar atmosphere, respectively.

Materials Characterization. X-ray diffraction (Bruker D8 ADVANCE) with Cu Kα radiation was employed to identify the composition and phase structure of the as-prepared Ni-based hybrids. Field emission scanning electron microscopy SEM (FESEM, SU8220, 20 kV) operating at 5 kV was used to characterize the morphology. TEM, HAADF-STEM, and elemental mapping images were recorded on an FEI Tecnai F20 transmission electron microscope. The valence state of the samples was investigated by X-ray photoelectron spectroscopy (XPS, Axis Ultra DLD, Kratos), using a monochromatic Al-Kα as radiation exciting source. N_2 adsorption/desorption isotherm was investigated at 77K with an automated gas sorption analyzer

(Micromeritics ASAP 2460). The carbon and power contents in the hybrids were determined by thermogravimetric analysis (TGA, TGA/DSC 3+, Switzerland) under Ar and air atmosphere with a heating rate of 10 °C min^{-1}, respectively.

Fabrication of half-cell and full-cell. The electrochemical performances of as-prepared YS Ni-based composites were performed via CR2025 coin-type cells. For fabrication of the working electrodes, the slurry of working electrodes consisted of 70 *wt* % active materials of the YS Ni-based composites, 20 *wt* % acetylene black, and 10 *wt* % polyvinylidene fluoride in methyl-2-pyrrolidone, which were mixed, then coated on Cu foil and dried at 80 °C under vacuum for 12 h. The mass loading of each working electrode was ~ 1.0 - 1.1 mg cm^{-2}. For sodium-ion batteries (SIBs) half-cell, sodium foil was the counter electrode, and the was the 1 M $NaClO_4$ in ethylene carbonate (EC)/diethyl carbonate (1:1, v/v) with 5 *wt* % fluoroethylene carbonate was used as the electrolyte. For potassium ion batteries (PIBs) half-cell, the potassium foil was employed as the counter electrode, and the electrolyte in the cell was 1 M KPF_6 in EC/propylene carbonate (1:1 v/v). SICs full cell was also fabricated with the optimized $Ni_2P_{0.75}S_{0.25}$/Ni@C/G as the anode and activated carbon (AC) as the cathode in the same electrolyte, and the mass ratio of cathode/anode was 3:1. A Whatman GF/F glass microfiber filter was used as the separator for SIBs, PIBs, and SICs.

Electrochemical testing. Galvanostatic discharge/charge (GDC) test and cycle-life tests were performed on a Land 2001A tester (Wuhan Land Electronics. Ltd.). Cyclic voltammetry (CV), GDC measurements of NICs, and electrical impedance spectroscopy (EIS) test from 100 kHz to 10 mHz. The specific capacitance (C, F g^{-1}), energy density (E, Wh kg^{-1}) and power density (P, W kg^{-1}) of NICs were calculated using the following equations [2, 3]:

$$C = I / [(dV / dt) \times m] \approx I\Delta t/m\Delta V,$$

$$E = 0.5\, CV^2$$

$$P = E/t$$

where I is the discharge current, Δt is the discharge time (s), m is the total mass of active material of the two electrodes, and V stands for working voltage, respectively.

Computational Methods. The first principle calculations have been employed to calculate the Na^+ ion adsorption energy and di□usion energy barrier of Ni_2P (111),

Ni_9S_8 (222), and layer-Ni_2P (111)-Ni_9S_8 (222) hetero-structure, respectively. The lattice mismatch was as follows: Δu = -4.94%, Δv = -3.17%. All calculations were based on density functional theory (DFT) and performed using the Cambridge Serial Total Energy Package (CASTEP) module, employing the ultra-soft pseudo-potential.[4] The exchange-correlation functional under the generalized gradient approximation (GGA) level was carried out using the Perdew-Burke-Ernzerhof (PBE) for solids functional.[5] The cut-o□ energy and the vacuum distance between the slabs were set to 517 eV and 20 Å, respectively. The Broyden-Fletcher-Goldfarb-Shanno scheme was employed as the minimization algorithm in the geometric optimization process until the force of each atom was smaller than 0.03 eV/Å.[6] The Brillouin zone was set as 3 × 3 × 1 *k*-grid, and the vacuum distance between the slabs was set to 20 Å.

In the computation of the Na^+ adsorption energy, the following equation was performed:

$$E_{ads} = E_{slab\text{-}substrate\text{-}Na+} - (E_{slab\text{-}substrate} + E_{slab\text{-}Na+})$$

where $E_{slab\text{-}substrate}$ and $E_{slab\text{-}Na+}$ are the total energy of the relaxed, isolated substrate slabs (Ni_2P (111), Ni_9S_8 (222), and Ni_2P(111)-Ni_9S_8(222) interface) and single Na^+ in the same slab, respectively. $E_{slab\text{-}substrate\text{-}Na+}$ *is* the total energy of the slab-substrate-Na^+ system. The migration barrier of Na-ion was conducted using the supercell by the complete LST/QST method in the CASTEP module.

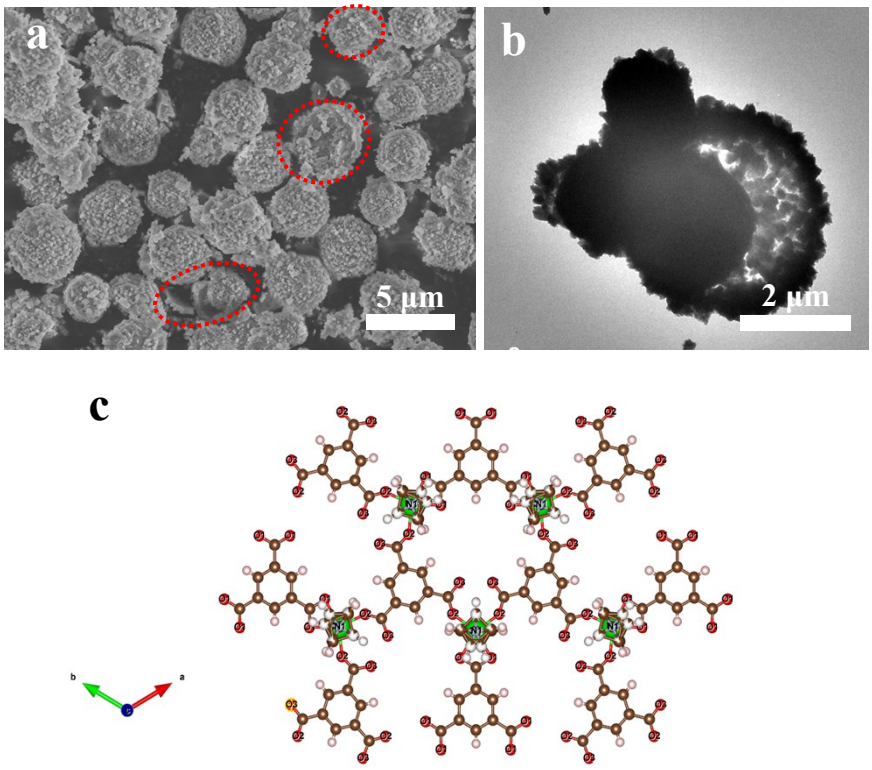

Figure S1 (a) SEM, (b) TEM image, and (c) Coordination environments of Ni^{2+} ions in the asymmetric units of Ni-MOF.

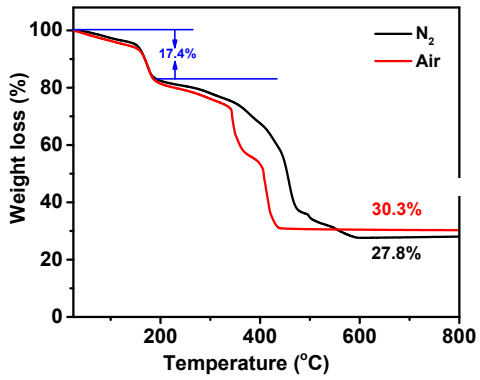

Figure S2 TGA-DSC curves of Ni-MOF in the Ar and air atmosphere.

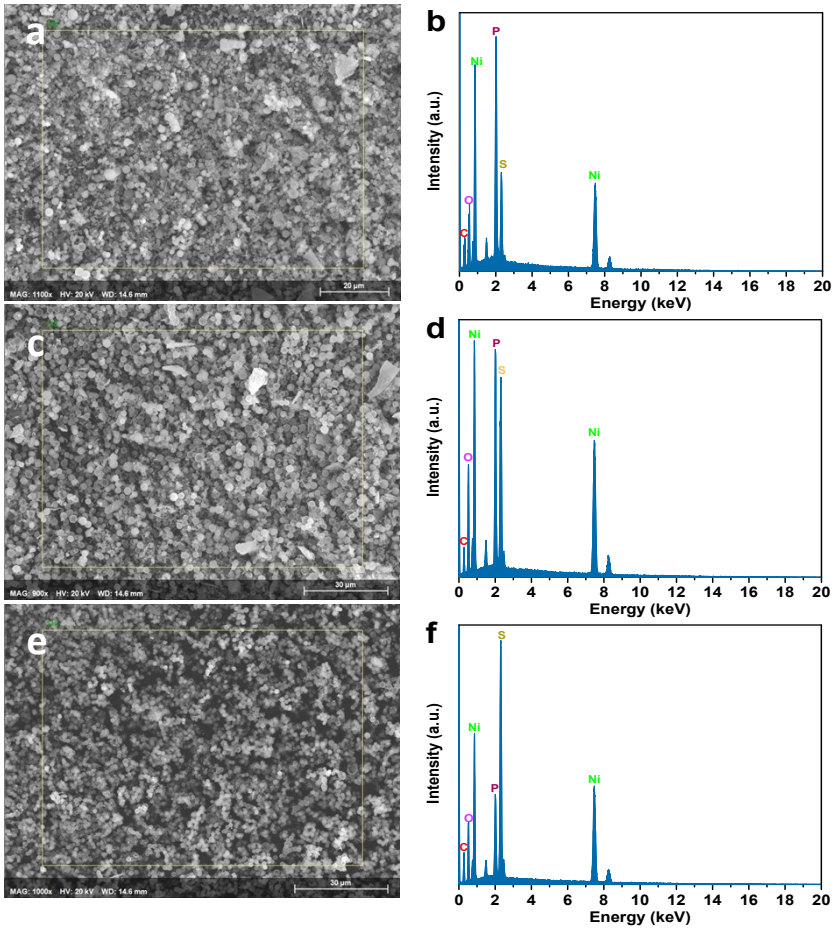

Figure S3 SEM images and EDX spectra of YS $Ni_2P_{1-x}S_x$/Ni@C/G, where (a, b), (c, d), and (e, f) correspond to x = 0.25, 0.42, and 0.53, respectively.

Table S1 The x value of the $Ni_2P_{1-x}S_x$/Ni@C/G determined by EDX.

Sample	X value	Mass weight	
		P power (g)	S power (g)
YS Ni_2P/Ni@C/G	0	0.080	0
YS $Ni_2P_{0.75}S_{0.25}$/Ni@C/G	0.25	0.053	0.027
YS $Ni_2P_{0.58}S_{0.42}$/Ni@C/G	0.42	0.040	0.040
YS $Ni_2P_{0.37}S_{0.53}$/Ni@C/G	0.53	0.027	0.053
YS Ni_9S_8/Ni@C/G	0.89	0	0.080

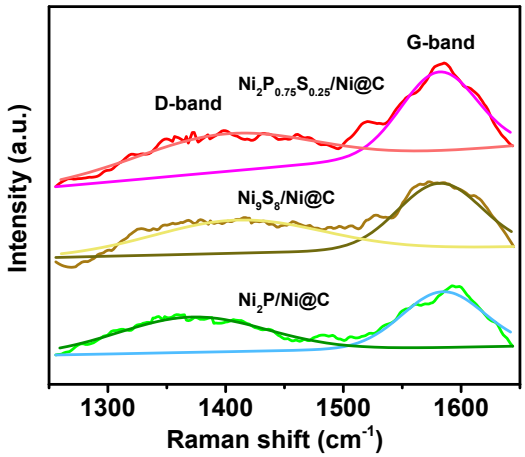

Figure S4 Raman spectra of Ni_2P/Ni@C/G, Ni_9S_8/Ni@C/G, and $Ni_2P_{0.75}S_{0.25}$/Ni@C/G, respectively.

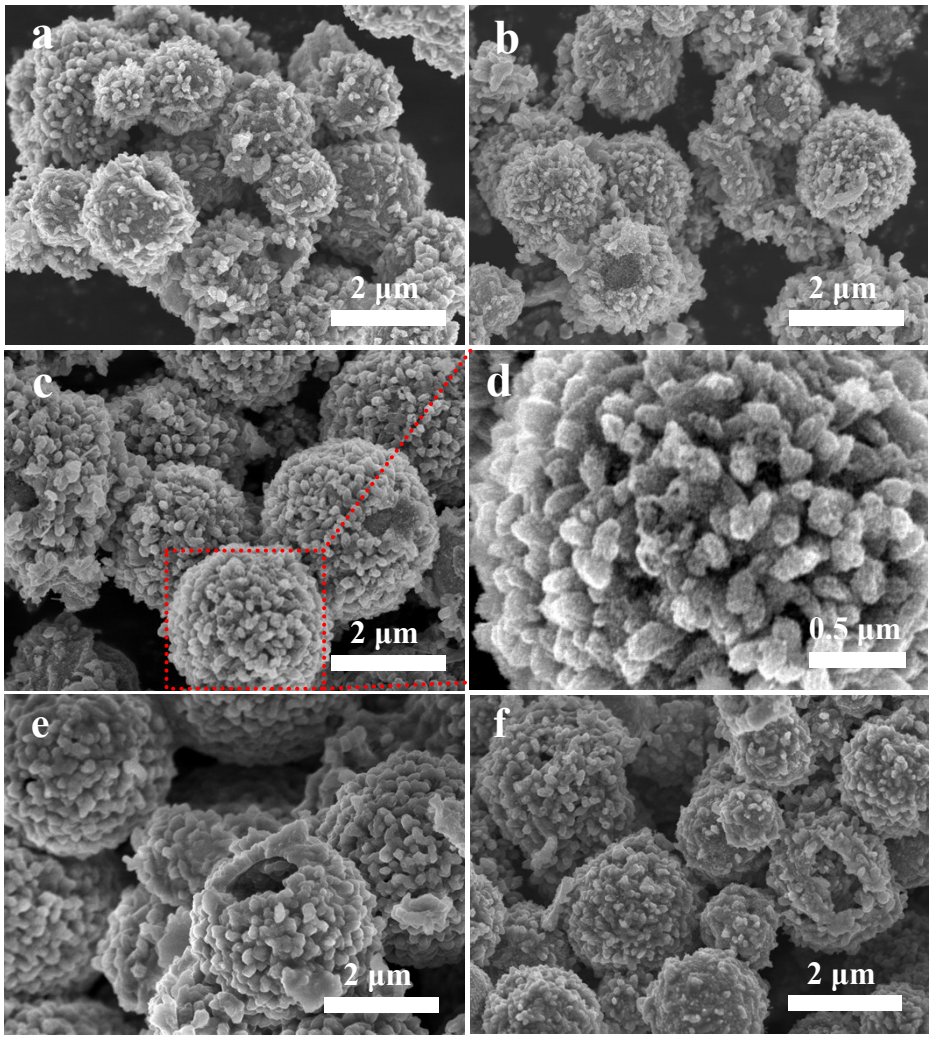

Figure S5 (a) SEM images of (a) YS Ni_2P/Ni@C/G, (b) YS Ni_9S_8/Ni@C/G, and (c-f) YS $Ni_2P_{1-x}S_x$/Ni@C/G, respectively.

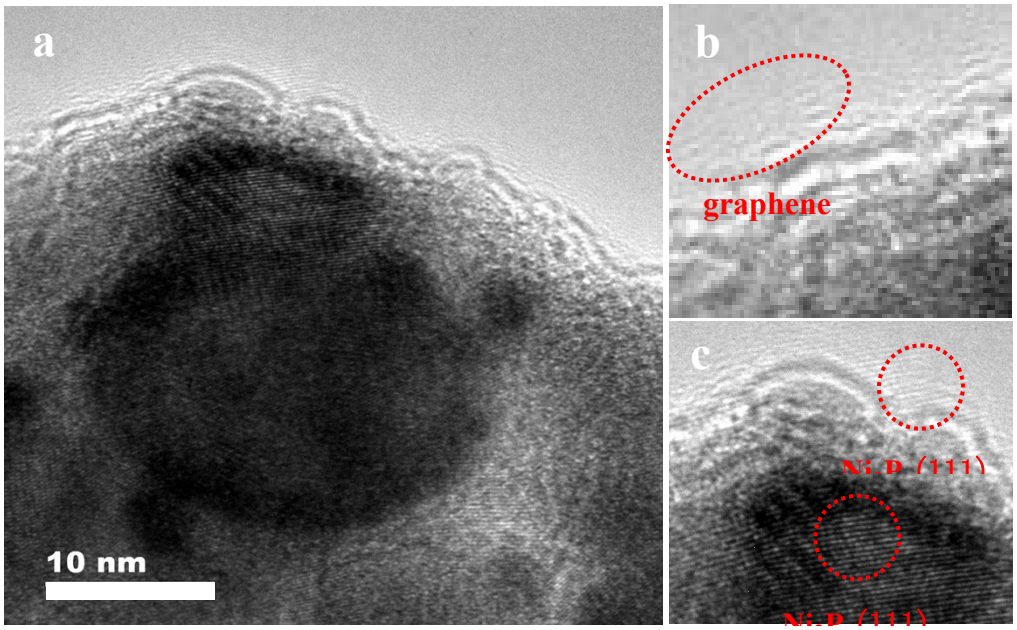

Figure S6 TEM images of YS $Ni_2P_{0.75}S_{0.25}$/Ni@C/G.

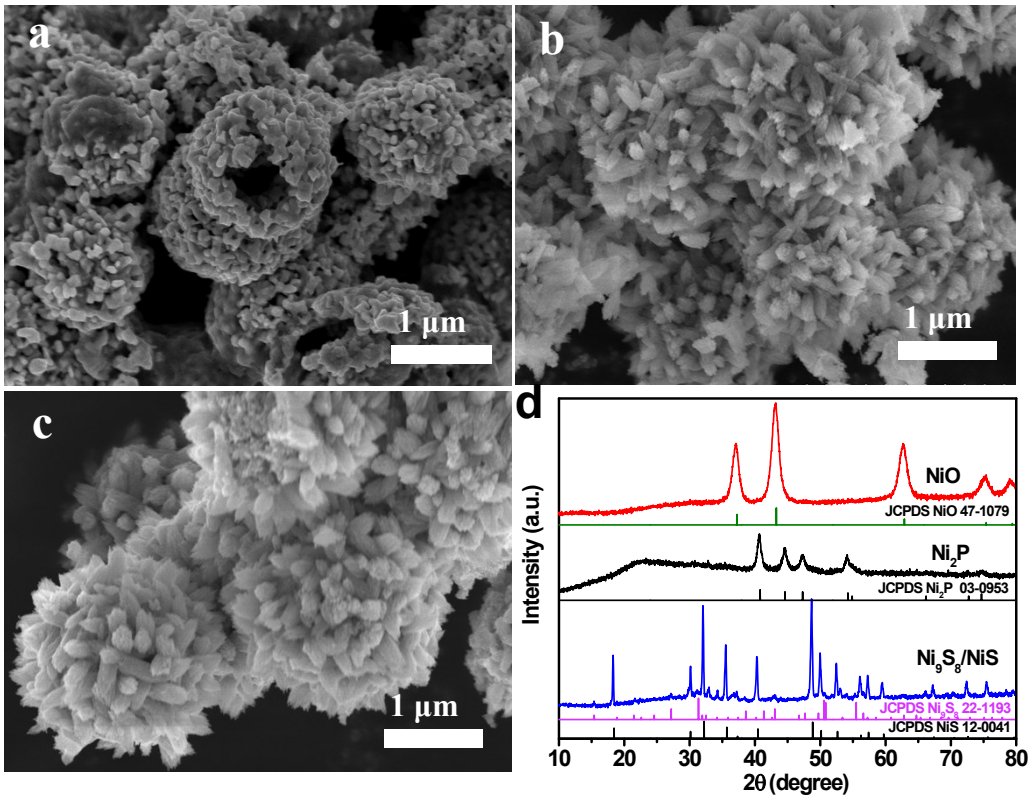

Figure S7 SEM images of porous (a) NiO, (b) Ni_2P, (c) Ni_9S_8/NiS, and (d) their corresponding XRD patterns, respectively.

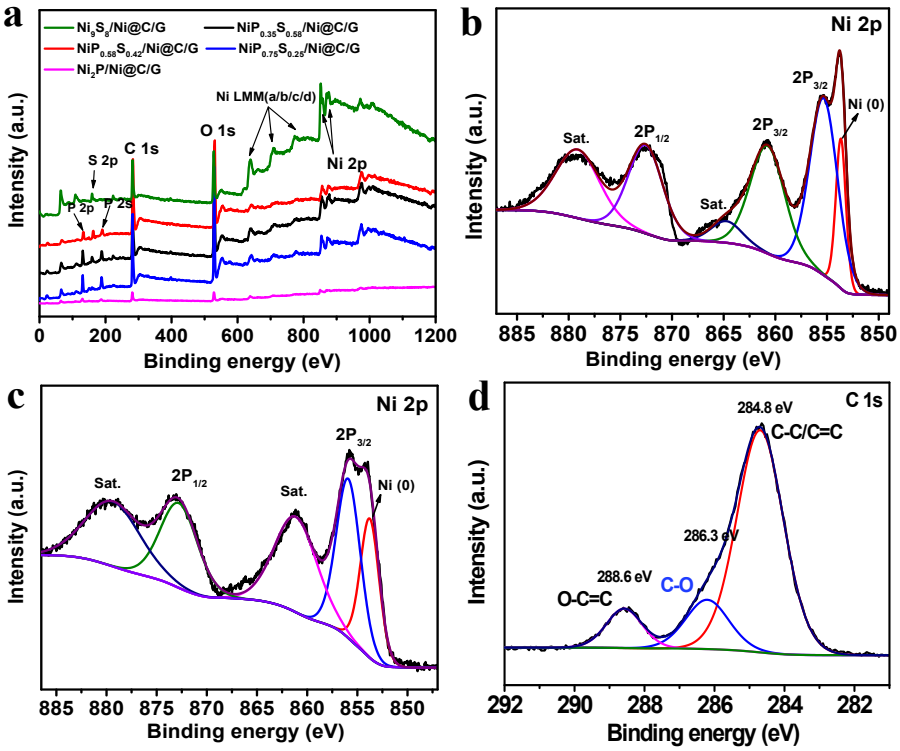

Figure S8 (a) XPS full survey spectra of YS $NiP_{1-x}S_x$/Ni@C/G, Ni_2P/Ni@C/G and Ni_9S_8/Ni@C/G, (b) Ni 2p in YS Ni_2P/Ni@C/G, (c) Ni 2p in YS Ni_9S_8/Ni@C/G, (d) C 1s in YS $Ni_2P_{0.75}S_{0.25}$/Ni@C/G.

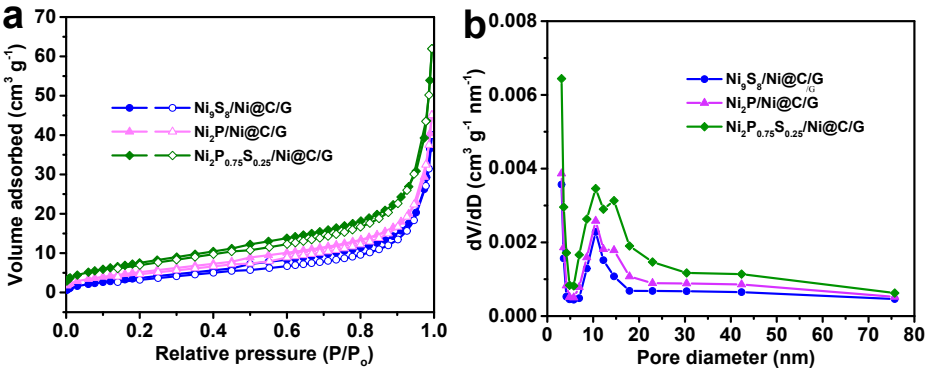

Figure S9 (a) N_2 adsorption-desorption isotherms and (b) pore-size distribution of YS Ni_2P/Ni@C/G, YS Ni_9S_8/Ni@C/G, and YS $Ni_2P_{0.75}S_{0.25}$/Ni@C/G, respectively.

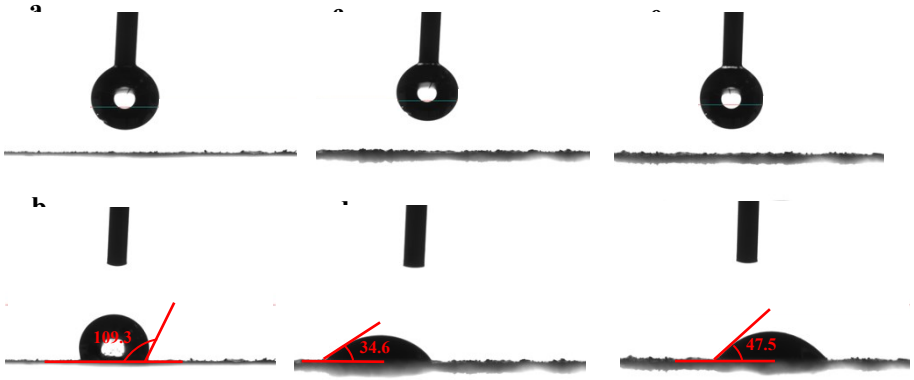

Figure S10 Surface wetting of H_2O droplet on (a, b) YS Ni_9S_8/Ni@C/G, (c, d) YS Ni_2P/Ni@C/G, and (d, f) YS $Ni_2P_{0.75}S_{0.25}$/Ni@C/G, respectively.

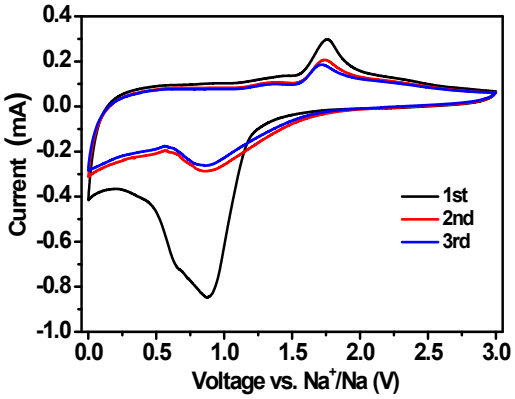

Figure S11 CV curves of YS $Ni_2P_{0.75}S_{0.25}$/Ni@C/G at a current density of 0.2 mV S^{-1}.

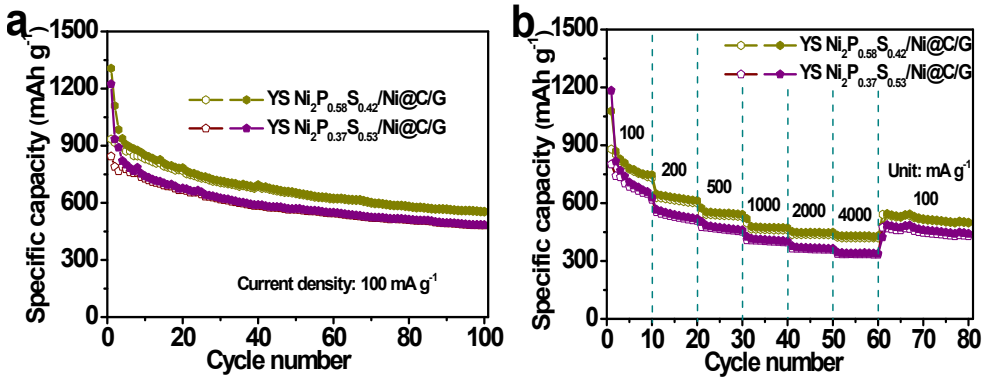

Figure S12 (a) Cycling stability at 100 mA g^{-1} and (a) rate capabilities of YS $Ni_2P_{0.58}S_{0.42}$/Ni@C/G and YS $Ni_2P_{0.37}S_{0.53}$/Ni@C/G for SIBs, respectively.

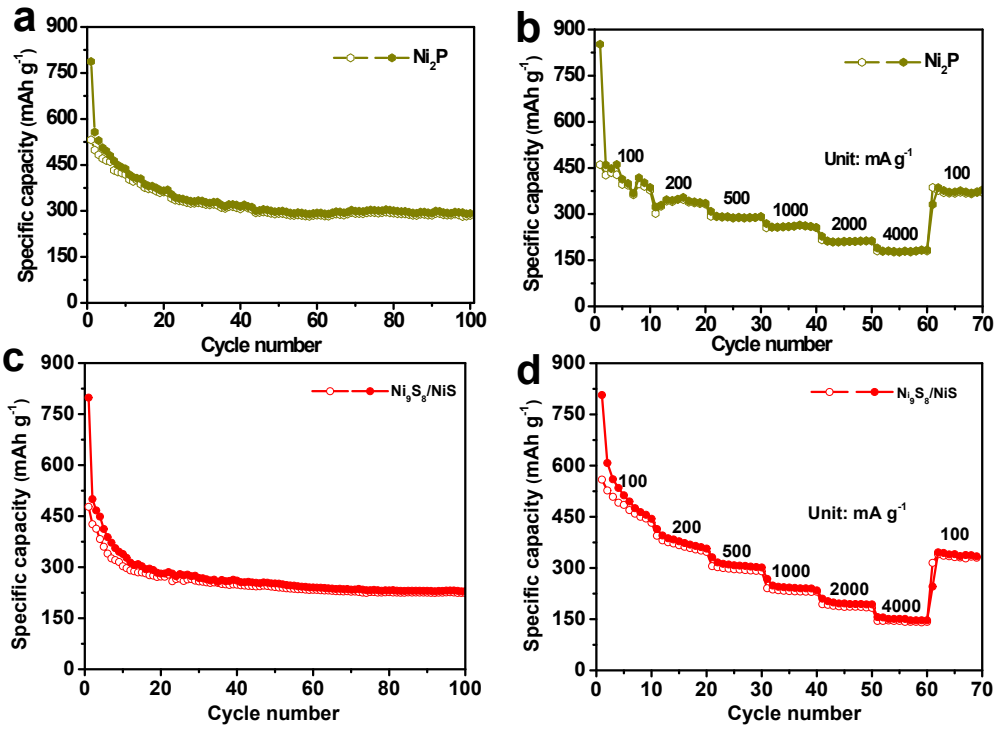

Figure S13 Cycling stability at 100 mA g^{-1} and rate capabilities of (a, b) Ni_2P, and (c, d) Ni_9S_8/NiS for SIBs, respectively.

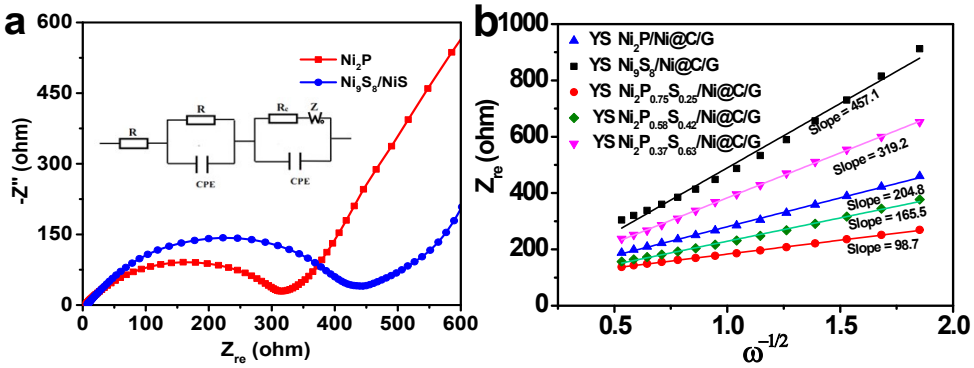

Figure S14 (a) Nyquist impedance plots of Ni_2P and Ni_9S_8/NiS after 100 cycles, and (b) the relationship plot between Z' and $\omega^{-1/2}$.

Table S2 Electrochemical impedance parameters of as-obtained Ni-based anodes for SIBs from equivalent circuit fitting of experimental data.

Sample	Cycle number	R_s/Ohm	R_f/Ohm	R_{ct}/Ohm
Ni_9S_8/NiS	100th cycle	5.7	109.3	319.0
YS Ni_9S_8/Ni@C/G	100th cycle	4.6	28.89	56.6
Ni_2P	100th cycle	5.4	107.8	208.1
YS Ni_2P/Ni@C/G	100th cycle	4.7	25.3	36.9
YS $Ni_2P_{0.75}S_{0.25}$/Ni@C/G	100th cycle	4.7	24.9	36.0
YS $Ni_2P_{0.58}S_{0.42}$/Ni@C/G	100th cycle	4.8	26.7	37.6
YS $Ni_2P_{0.37}S_{0.63}$/Ni@C/G	100th cycle	4.6	26.4	38.3

Equations (1) and (2):

$$D = \frac{R^2T^2}{2A^2n^4F^4c^2\sigma_w^{\ 2}} \quad (1) \qquad Z' = R' + \sigma_w\omega^{-1/2} \quad (2)$$

Where R is the gas constant, T is the absolute temperature, A is the surface area of the electrode, n is the number of transferred electrons per molecule, F is the Faraday constant, c is the molar concentration of Na^+ ions, R' mainly involves the interface impedance and charge transfer resistances for these electrodes, ω ($\omega = 2\pi f$) is the angular frequency, and σ_w is the Warburg factor ($Z' \propto \sigma_w\omega^{-1/2}$), respectively.

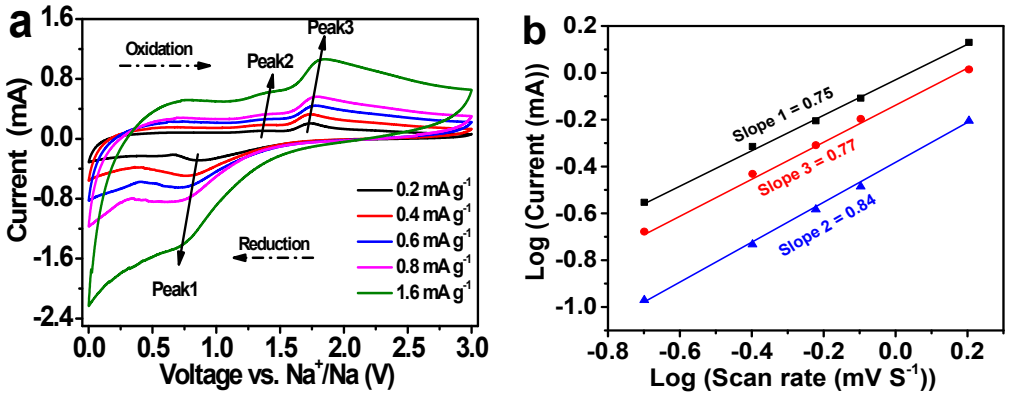

Figure S15 (a) CV scans of YS $Ni_2P_{0.75}S_{0.25}$/Ni@C/G at various rates and (b) correspondingly fitted b-value at respective redox peaks for SIBs anode.

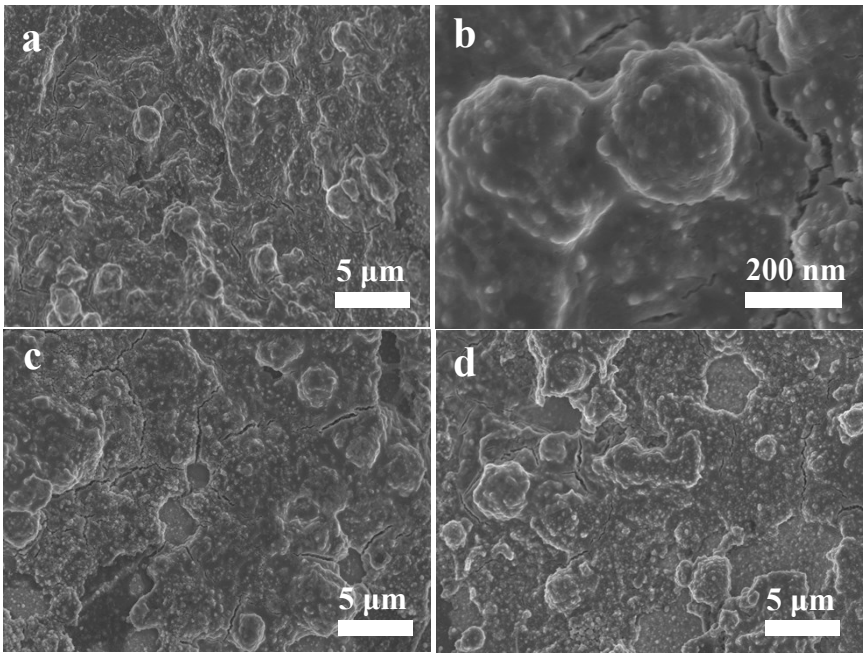

Figure S16 SEM images of (a, b) YS $Ni_2P_{0.75}S_{0.25}$/Ni@C/G, (c) YS $Ni_2P_{0.58}S_{0.42}$/Ni@C/G and (d) YS $Ni_2P_{0.37}S_{0.53}$/Ni@C/G after 100 cycles at 100 mA g^{-1}, respectively.

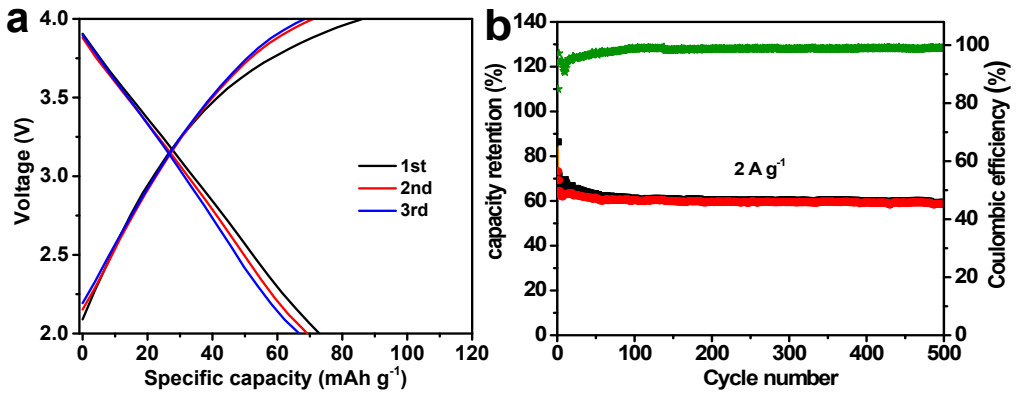

Figure S17 (a) GCD curves, and (b) cycle performance at 2 A g^{-1} of the AC cathode for Na-storage.

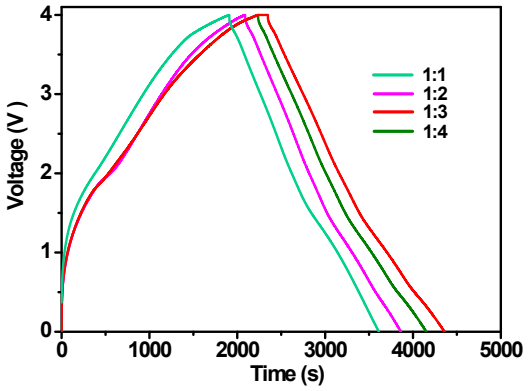

Figure S18 GDC curves of SICs with different mass ratios (anode: cathode, 1:1, 1:2, 1:3, and 1:4) at a current density of 0.5 A g^{-1}.

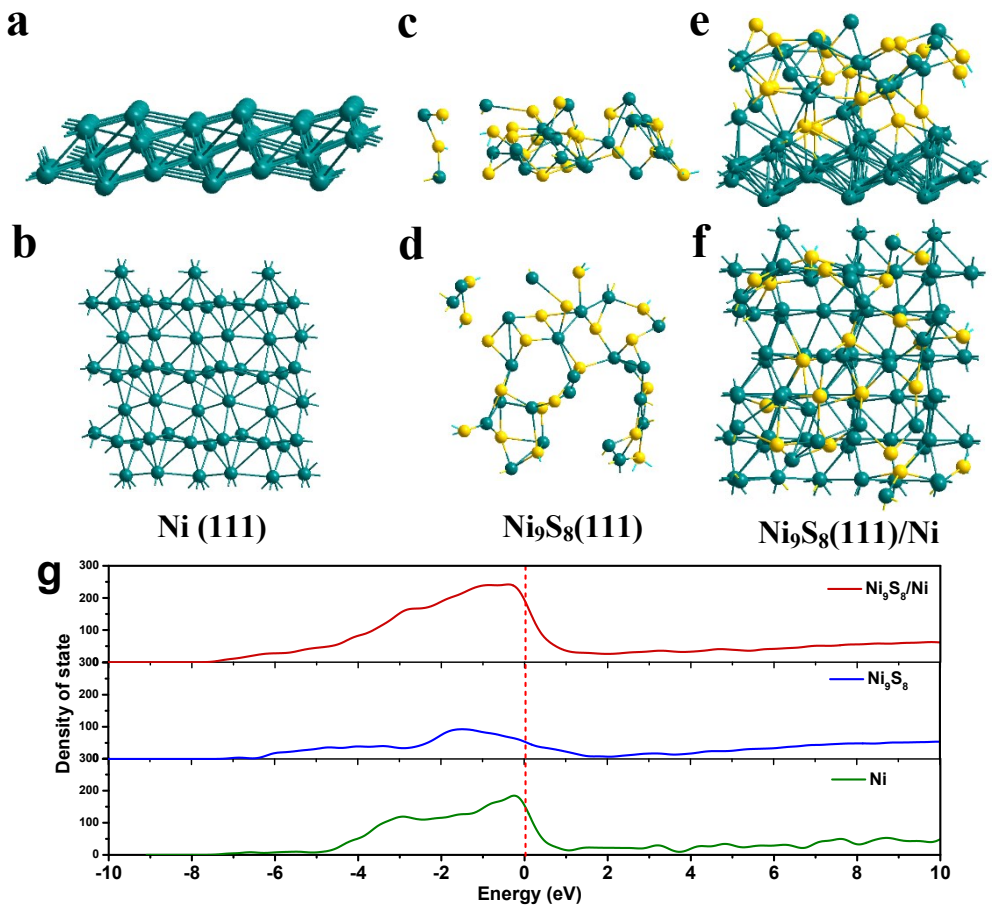

Figure S19 (a, c, e) Side-, and (b, d, f) top-views schematic model of the Ni (111), Ni_9S_8 (222), and the Ni_9S_8 (222)-Ni, and (g) DOS curves for Ni (111), Ni_9S_8 (222), and the Ni_9S_8 (222)/Ni.

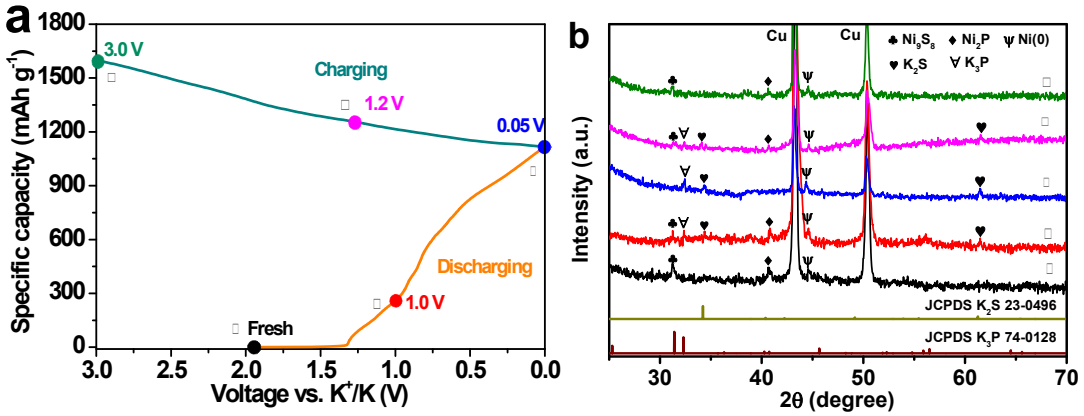

Figure S20 (a) The first charge-discharge profile and (b) its corresponding ex-situ XRD patterns of YS $Ni_2P_{0.75}S_{0.25}$/Ni@C/G anode in PIBs at the different voltage platforms.

Table S3 Performance comparison of between $Ni_2P_{0.75}S_{0.25}$/Ni@C/G and the reported anode materials for PIBs

Sample	Cycling performance (mAh g^{-1})/cycle number, current density (mA g^{-1})	Rate capability (mAh g^{-1})/current density (mA g^{-1})	Reference
$Ni_2P_{0.75}S_{0.25}$/Ni@C/G	**372/200, 150**	**238/3200**	**This work**
NiS_2@C@C	303/100, 50	151/1610	*Adv. Funct. Mater. 2019, 29, 1903454*
ZnSe-$FeSe_2$/RGO	363/100, 50	--	*J. Power Sources 2020, 455, 227937*
Y-S NiS_x@C	364/200, 100	232/2000	*J. Mater. Chem. A, 2019, 7, 18932*
mp-Co_9S_8@C/rGO	408/100, 200	278/2000	*Nano Res. 2020, 13, 802-809*
Fe-Ni-P hollow nanoframes	60/700, 200	46/2000	*Chem. Eng. J. 2020, 390, 124515*
FeS_2@G@CNF	205/100, 200	171/1000	*Small 2019, 15, 1804740*
Hollow V_2O_3@C sphere	330/500, 100	125/2000	*J. Mater. Chem. A, 2020, 8, 13261*
r-SnP@C	355/300, 100	258/1000	*Carbon 2020, 168, 468-474*
CoP⊂NPPCS	127/1000, 100	54/2000	*Adv. Mater. 2018, 30, 1802310*
TiO_xN_y/C	125/100, 200	72/1600	*Chem. Eng. J. 2019, 369, 828-833*
N/O Dual-dope hard Carbon-800	305/100, 100	223/2000	*Adv. Sci. 2020, 7, 1902547*
SnO_2@CF	399/150, 100	247/2000	*Energy Environ. Sci., 2020,13, 571-578*
NC@CoP/NC	279/100, 100	200/2000	*Small 2020, 16, 1906566*

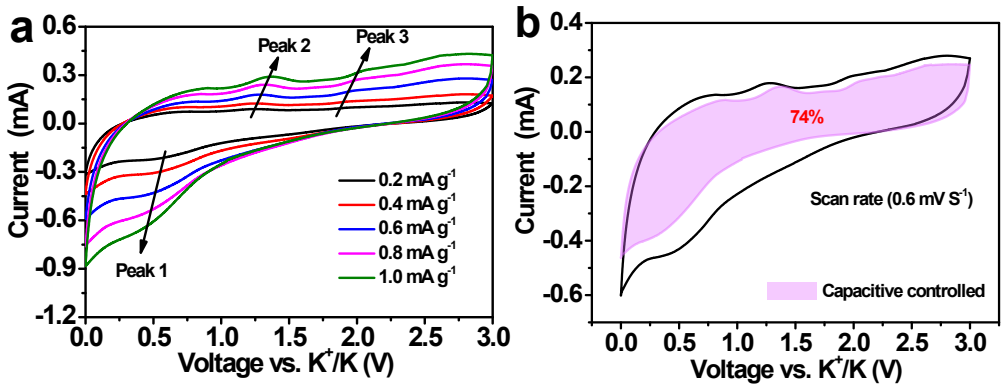

Figure S21 (a) CV scans of YS $Ni_2P_{0.75}S_{0.25}$/Ni@C/G at various rates, and (b) the shaded region shows the CV profile with the capacitive contribution at a scan rate of 0.6 mV s^{-1} for PIBs anode.

References:

1. F. Zou, Y. M. Chen, K. Liu, Z. Yu, W. Liang, S. M. Bhaway, M. Gao and Y. Zhu, *ACS Nano*, 2016, **10**, 377-386.
2. H. Kim, M.-Y. Cho, M.-H. Kim, K.-Y. Park, H. Gwon, Y. Lee, K. C. Roh and K. Kang, *Adv. Energy Mater.*, 2013, **3**, 1500-1506.
3. J. L. Rutao Wang, Peng Zhang, Zongyuan Lin , Xingbin Yan, *Adv. Funct. Mater.*, 2015, **25**, 2270–2278.
4. D. Vanderbilt, *Phys. Rev. B*, 1990, **41**, 7892–7895.
5. J. P. Perdew, A. Ruzsinszky, G. I. Csonka, O. A. Vydrov, G. E. Scuseria, L. A. Constantin, X. Zhou and K. Burke, *Phys. Rev. Lett.*, 2008, **100**, 136406.
6. B. G. Pfrommer, M. Côté, S. G. Louie and M. L. Cohen, *J. Comput. Phys.*, 1997, **131**, 233-240.